small methods

www.small-methods.com

Lignin-Derived Holey, Layered, and Thermally Conductive 3D Scaffold for Lithium Dendrite Suppression

*Daxian Cao, Qing Zhang, Ahmed M. Hafez, Yucong Jiao, Yi Ma, Hongyan Li, Zheng Cheng, Chunming Niu, and Hongli Zhu**

Lithium (Li) metal anodes are considered as the holy grail of rechargeable Li batteries. However, the practical utilization of Li metal is challenging because of the dendrite formation issue and drastic volume expansion. Herein, for the first time, through the incorporation of thermally conductive material boron nitride (BN), the Li metal anode is stabilized by improving heat dissipation and charge transfer in a holey and layered structure. Ligninsulfonate, due to its amphiphilicity, is used to in situ exfoliate bulky BN into nanosheets. Through the freeze-casting method, a layered and holey structure is formed, where the as-exfoliated BN nanosheets can well manage thermal distribution and lead to a uniform deposition of Li. Due to the enhanced thermal dissipation and charge transference, this novel Li anode exhibited a high Coulombic efficiency and a long cycle life at a high current density of 4 mA cm^{-2}. And the formation of Li dendrite is successfully suppressed during plating/stripping. In a full cell where $LiFePO_4$ composite was used as the cathode, a high capacity of 90 mAh g^{-1} was achieved at 10 C with a high capacity retention of 92% after 1800 cycles.

Lithium (Li) metal has been considered as the most promising anode material for rechargeable Li batteries due to its light weight (0.59 $g \cdot cm^{-3}$), lowest reduction potential (−3.04 V vs standard hydrogen electrode), and highest theoretical specific capacity (3860 $mAh \cdot g^{-1}$).[1] However, challenges such as unstable solid electrolyte interface (SEI), drastic volume expansion upon repeated charge/discharge, and uncontrollable growth of Li dendrite remain to impede commercialization of Li metal–based batteries.[2] Consequenced from these challenges, the dendrite formation particularly causes low Coulombic efficiency and poor stability of the battery and potentially triggers severe safety problems.[3] The growth of dendrite causes inhomogeneous deposition of Li, and heat dissipation is a key factor to control the uniform thermal distribution and improve the Li plating/stripping uniformity. At high current density, the drastic joule heat generated on the surface will bring faster Li ion deposition/dissolution. Inefficient thermal dissipation, especially in the sharp position, leads to the non-uniform thermal distribution and thus cause more severe dendrite formation. There is limited work elucidating the effect of thermal distribution on the dendrite formation of Li metal anodes. Hu and co-workers coated one layer of thermally conductive boron nitride (BN) on the separator, and also fabricated a novel separator composed of poly vinylidene fluoride-hexafluoropropene (PVDF-HFP) and BN. In both ways, heat was distributed more evenly, and Li dendrite growth was suppressed successfully.[4] However, since their efforts were made on the separator part, the thermal dissipation was limited and the huge volume change of Li during the plating/stripping process was not mitigated, which greatly affected the battery performance.

Meanwhile, a variety of approaches have been reported to address or alleviate the dendrite issue, among which introducing a 3D structure to host Li has been proved to be an effective method to suppress the dendrite growth. In the prior reports, the 3D structures can provide an enlarged contact area between Li and electrolyte, which is favorable for reducing the local current density and enhancing the mobility of Li ions.[5] However, in those studies, the effective area for electrochemical reaction in the 3D structures was fully optimized and ion accessibility was limited, as the host structures were densely filled with Li and there was limited space to buffer the volume change.[6]

In this work, for the first time, we introduce a layered and holey carbon (LHC) scaffold with enhanced thermal diffusivity and superior ion accessibility to stabilize the Li metal electrode. BN with a hexagonal structure has high mechanical strength, high chemical stability, and excellent thermal conductivity, and it is often used to control thermal distribution of electronics.[7] Compared with bulky BN, the basal-plane thermal conductivity of the monolayer BN can achieve 2000 $W\ m^{-1}\ K^{-1}$ at room temperature, which inspires many approaches to exfoliate bulky BN into monolayer or few-layer structure to obtain a high thermal conductivity.[8,9] We utilized the ligninsulfonate (SL) to exfoliate

D. Cao, Dr. Q. Zhang, A. M. Hafez, Dr. Y. Jiao, Y. Ma, Dr. H. Li, Z. Cheng, Prof. H. Zhu
Department of Mechanical and Industrial Engineering
Northeastern University
360 Huntington Avenue, Boston, MA 02115, USA
E-mail: h.zhu@neu.edu

D. Cao, Prof. C. Niu
Center of Nanomaterials for Renewable Energy (CNRE)
State Key Lab of Electrical Insulation and Power Equipment
School of Electrical Engineering
Xi'an Jiaotong University
Xi'an 710049, China

DOI: 10.1002/smtd.201800539

the bulky BN into few-layer nanosheets. Extracted from trees, SL is one of the most abundant biomaterials with an annual production of 9.8×10^5 tons in the paper manufacturing process. However, they are mostly used as fuel without much further utilization for other purposes.[10] With the hydrophobic backbone of hyperbranched macromolecular and hydrophilic branches of sulfonate, SL can work as a surfactant to exfoliate bulky 2D materials into nanosheets and stabilize their aqueous dispersion.[11] After the exfoliation process, the LHC/BN scaffold is obtained through a freeze-casting method followed by a carbonization process. When being applied as the host for Li, this layered and holey structure delivered advantages: 1) Compared with the layered structure formed through vacuum filtration which has interlayer gaps in nanometer scale, the interlayer gaps of LHC/BN are in micrometer scale. The large interlayer gaps are favorable for large amount of Li deposition, as well as accommodation of volume expansion and thermal dissipation during cycling.[12] 2) The holes formed in the layers could enhance the accessibility of electrolyte and thus promote the ion transfer. 3) The BN nanosheets could homogeneously distribute heat on the surface of the carbon layer, and enable uniform nucleation and growth of Li. This work will motivate more research efforts on the study of thermal dissipation of Li metal anodes.

Figure 1a schematically illustrates the exfoliation process of BN using SL. The SL used in this study has a molecular weight of 4000 $g \cdot mol^{-1}$, and there are hydrophilic groups, including sulfonic, carboxyl, and phenolic hydroxyl groups, on the hydrophobic carbon backbone, as shown in Figure S1 in the Supporting Information.[13] Using ultrasonic treatment, the SL

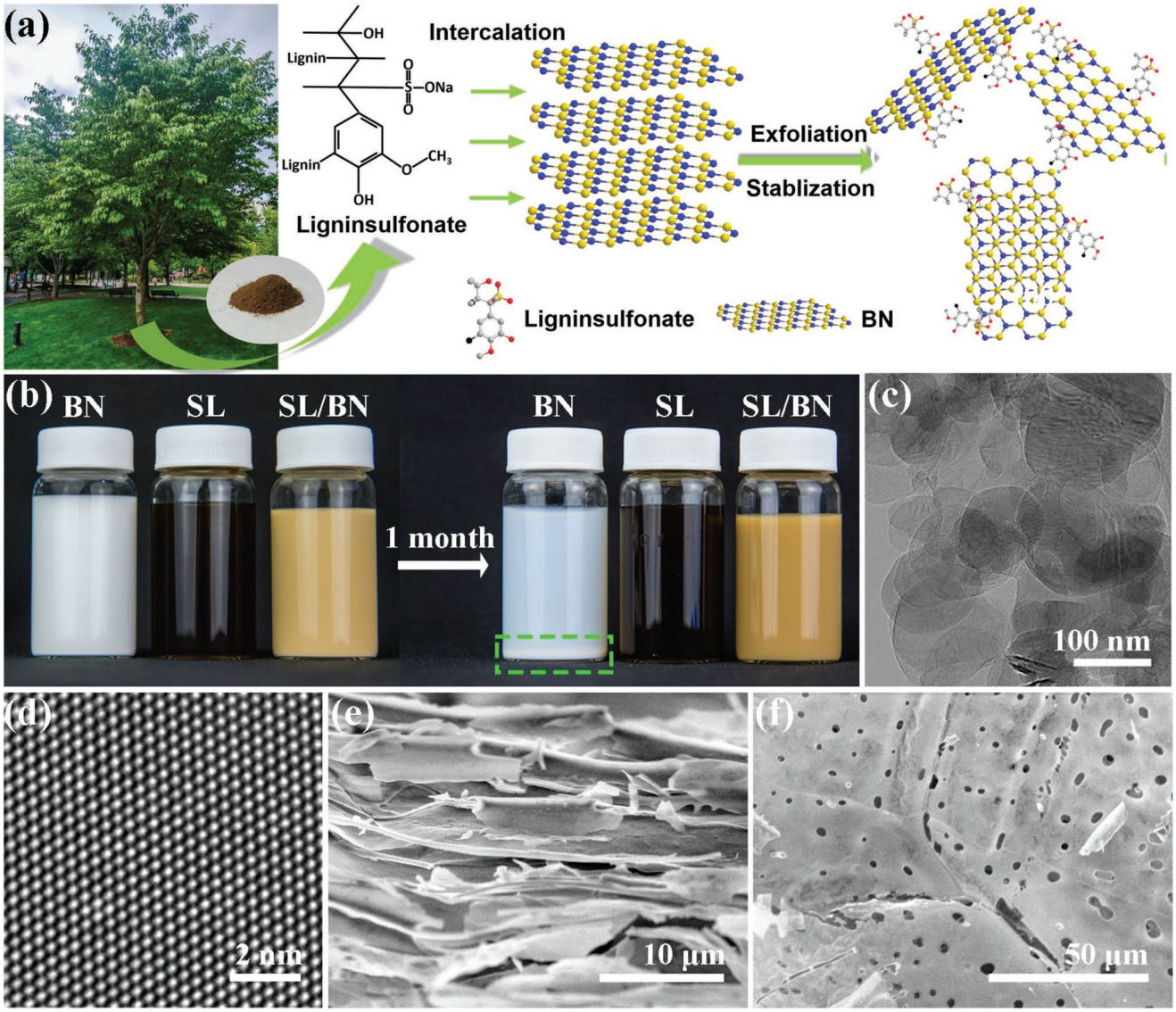

Figure 1. Exfoliation of BN with SL and the preparation of SL/BN through freeze-casting. a) Schematic representation of the exfoliation of BN using SL. The inset figure shows the optical image of SL powder. b) Optical images of BN, SL, and SL/BN dispersed in water as-prepared and after storing for 1 month. c) TEM image of exfoliated BN nanosheets. d) HRTEM image of the exfoliated BN nanosheet. e) SEM image of cross-section SL/BN, and f) SEM image of the surface of SL/BN.

molecules can intercalate into the space between the layers of 2D BN, and exfoliate the bulky BN into nanosheets. The exfoliated BN nanosheets were surrounded by the SL and gathered into micelles, thus a stable dispersion was then formed.

Figure 1b compares optical photographs of BN, SL, and SL/BN dispersed in water before and after storing for 1 month, respectively. Due to the hydrophobic property, BN had a poor dispersion in water, and there was obvious precipitation after 1 month. In contrast, SL aqueous solution and SL/BN dispersion remained well-dispersed without any precipitation, which suggested that the SL can promote the dispersion of BN in water. To evaluate the stability of this aqueous dispersion, dynamic light scatter (DLS) was used to measure the particle size distribution and polydispersity index (PDI) (Figure S2, Supporting Information).[14] After the exfoliation process, the average size of the particles in BN dispersion increased from 116.9 to 228.5 nm, and the corresponding PDI decreased from 0.344 to 0.176. This result revealed that SL not only exfoliated BN, but also bonded them together into micelle of larger size, which could disperse better in aqueous solution. Transmission electron microscopy (TEM) and high-resolution TEM (HRTEM) were used to characterize the BN and SL/BN before and after exfoliation. As shown in Figure S3a in the Supporting Information, the pristine BN powder showed a thick flake-like shape. After adding the SL and sonication, thinner BN nanosheets were obtained with amorphous matrix surrounding (Figure S3b, Supporting Information). The TEM data were in agreement with the DLS results of the increased average particle size. As illustrated in Figure 1c, after rinsing with water, the SL was removed and few-layer BN nanosheets were obtained, and the thickness of BN was reduced based on the transparency of the particles. HRTEM image in Figure 1d clearly illustrates the honeycomb atomic structure of BN, confirming the exfoliation of BN into few layers.

A layered and holey structure attached with BN nanosheets was obtained after a freeze-casting process (shown in Figure S4 in the Supporting Information). Scanning electronic microscope (SEM) was used to characterize the morphology. From the cross-section image, the aerogel had stacked layers with interlayered gap over 1 μm (Figure 1e). From the top view in Figure 1f, it can be seen that there were plenty of holes on each layer. The formation of the layered structure can be ascribed to the growth of ice crystals. SL was rejected from the ice and accumulated into layers during the freezing process. BN was firmly attached to the layers in situ, and the holes in the layers were formed due to the sublimation of ice.

Figure 2a shows an optical image of free-standing LHC/BN electrode. And the SEM image in Figure 2b shows the surface morphology of the LHC/BN, and it was composed of layers with size larger than 300 μm. Every single layer is holey and wavy (Figure 2c). From the cross-section SEM images of different magnifications (Figure 2d–f), it is obvious that the layered and holey structure was well-preserved after carbonization, with a spacing over 10 μm between the adjacent layers. In addition, the surface area and pore size distribution were detected through the N_2 adsorption–desorption isotherms (Figure S5, Supporting Information). The LHC/BN has a large surface area of 261.9 $m^2\ g^{-1}$ and a pore size distribution from several nanometers to tens of nanometers.

TEM was used to investigate morphologies of the exfoliated BN nanosheets and carbon layers derived from SL. After carbonization, the layered carbon was mostly amorphous with partial graphitization at the edge (Figure S6, Supporting Information). As shown in Figure 2g, BN nanosheets densely covered the surface of the amorphous carbon, indicating strong bonding formed between the SL and the BN during the exfoliating process. The few-layer BN nanosheets showed overlapping, Figure 2h. The overlapping of BN has been proved to be beneficial for phonon transfer and thermal conductivity.[9] A clear lattice d-spacing of 0.217 nm was observed in the HRTEM image, which corresponded to the (100) plane of BN (Figure 2i). Additionally, the dashed line shows a distinct boundary between the few-layer BN nanosheet and the amorphous carbon.

Raman and X-ray diffraction (XRD) measurements also confirmed that the as-exfoliated BN was well-crystallized and the carbon was amorphous with partial graphitization (Figures S7 and S8, Supporting Information). In Figure 2j, it is hard to distinguish the monolayer BN from the carbon base because of the amorphization of carbon. In the fast Fourier transform (FFT) data in the inset, the bright hexagonal confirms the existence of monolayer BN and the circle area is related to the amorphous carbon.

To evaluate the enhancement in thermal dissipation after introducing BN, the thermal diffusivities of both LHC and LHC/BN were measured using laser flash method. The principle of the measurement is schematically illustrated in **Figure 3**a. A laser pulse heats one side of a pelletized sample, and an infrared detector collects the time-dependent temperature signals from the opposite side of the sample. Higher thermal diffusivity will lead to faster temperature rise. Figure 3b shows the temperature signals of LHC and LHC/BN detected as a function of the time, and they were fit with "Cape-Lahman + pulse correction model." It is obvious that, compared to LHC, with the addition of BN, halftime $t_{1/2}$ decreased significantly from 538.95 to 65.25 ms. Calculated from equation "$\alpha = 0.1388\ d^2/t_{1/2}$" (where d is the thickness, 1.15 mm), with the presence of BN, the corresponding thermal diffusivity α remarkably increased by a factor of 8 from 0.34 to 2.81 $mm^2\ s^{-1}$.

Figure 4 shows the Coulombic efficiency of LHC/BN, LHC, and Cu electrode in the Li plating/stripping test. Li with an areal charge of 1 $mAh \cdot cm^{-2}$ was deposited onto the three electrodes, respectively, at the current density of 1 $mAh \cdot cm^{-2}$, and then stripped away with a cutoff voltage of 1 V. The plating/stripping process was repeated several times. As shown in Figure 4a, LHC/BN had a stable Coulombic efficiency of 98.5% over 500 cycles. Without BN, the Coulombic efficiency of the LHC maintained 97% for 400 cycles, and dropped to 60% quickly after the first 400 cycles. As a comparison, the Coulombic efficiency of Cu electrode showed significant variations in the range of 80–110%. This unstable Coulombic efficiency implied an unstable Li plating/stripping process and the gradual formation of dendrite.[15] The Coulombic efficiency data suggested that the layered structure without BN can stabilize the Li to some extent, but the stabilization was limited and dendrite still formed over continued cycling.

The inset images show the voltage profiles of the 5th, 150th, and 500th cycle, respectively. The Li started to plate when

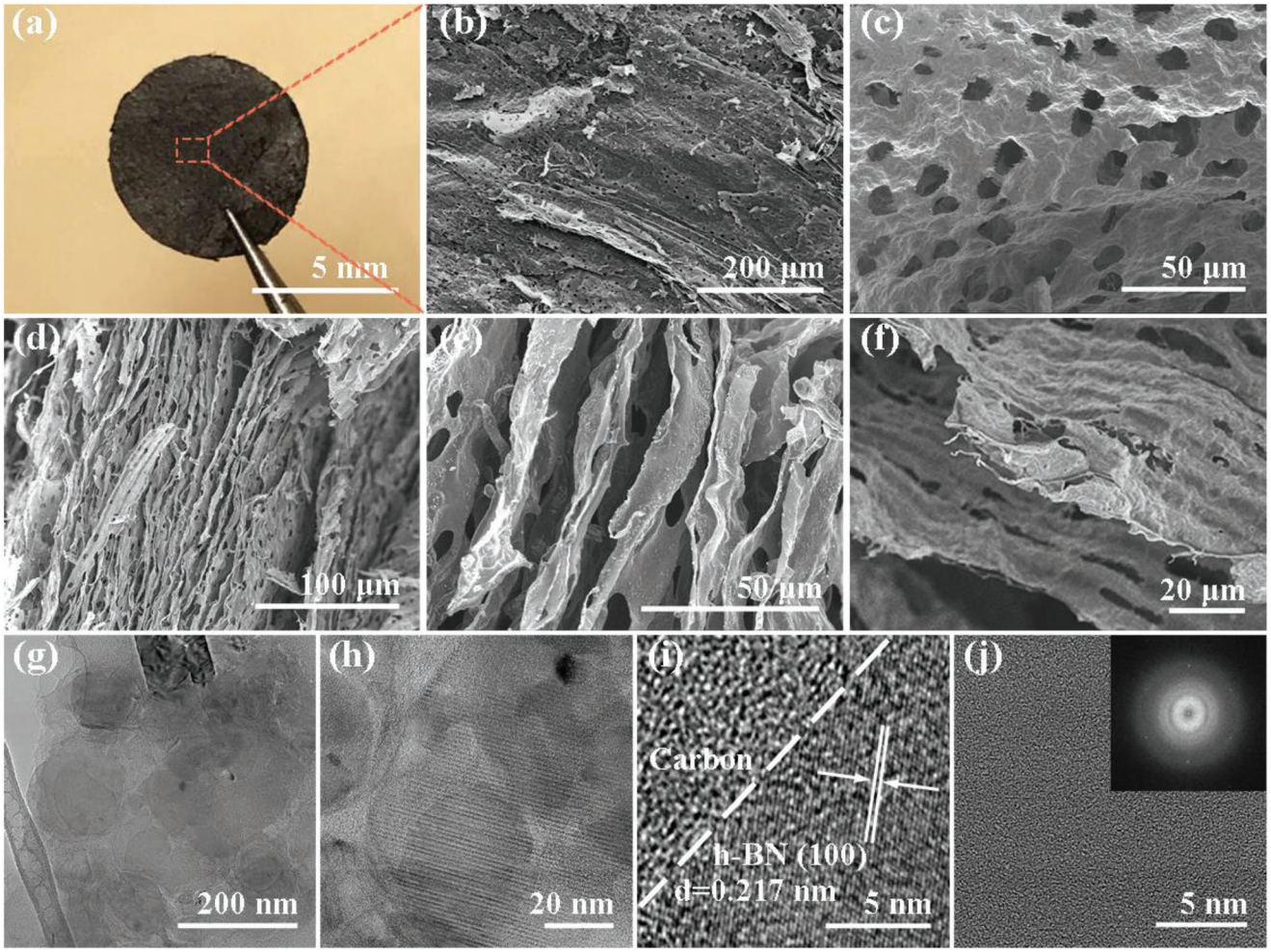

Figure 2. Morphology characterization of LHC/BN. a) Photograph and (b) surface SEM image of the LHC/BN electrode. c) Surface SEM image of single-layered LHC/BN. d) Cross-section and e) zoom in SEM images of LHC/BN electrode. f) Cross-section SEM of single-layered LHC/BN. TEM images of LHC/BN at g) high and h) low magnification. HRTEM images of i) few-layer BN nanosheet and j) single layered BN nanosheet on the carbon in LHC/BN. The inset shows the FFT data.

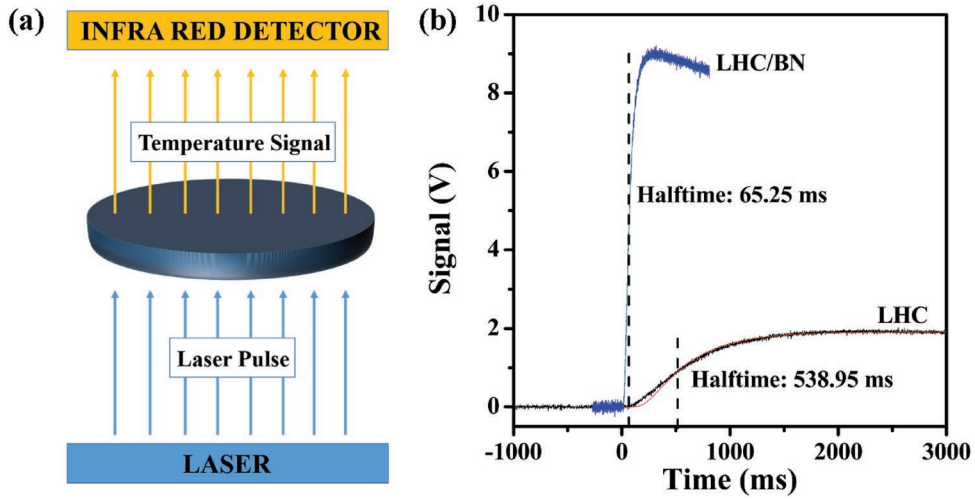

Figure 3. a) Schematics of laser flash method. b) Temperature profiles to calculate the thermal diffusivity of LHC/BN and LHC.

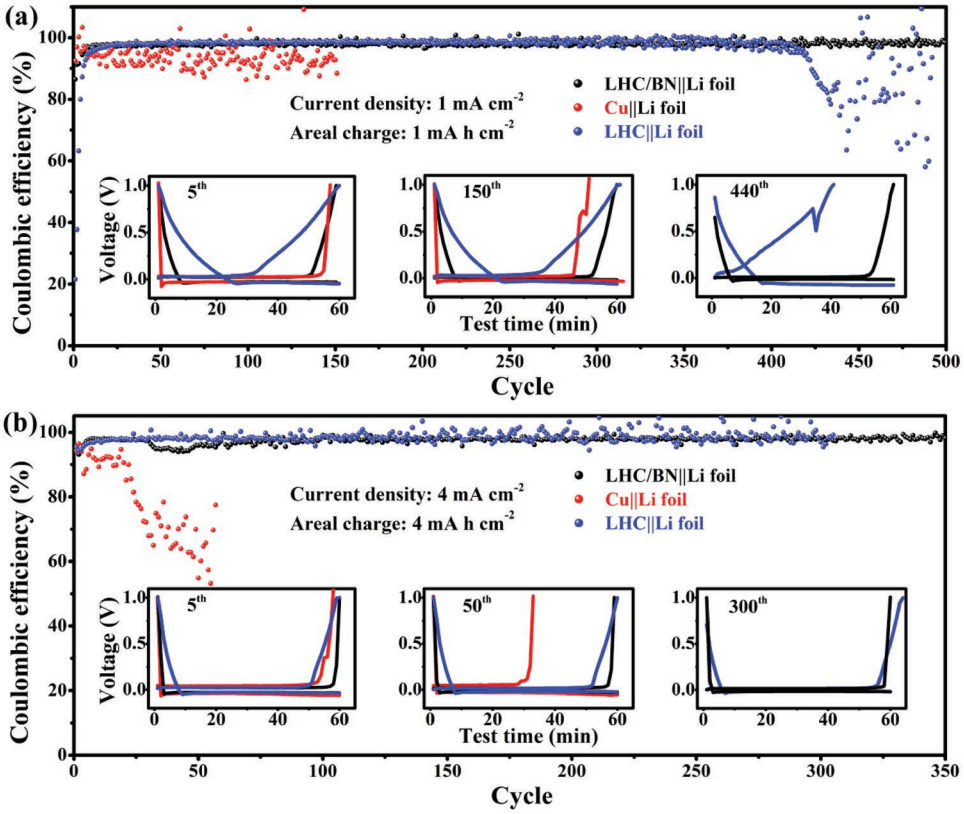

Figure 4. Comparison of Coulombic efficiency between LHC/BN, LHC, and Cu electrodes (a) with an areal charge of 1 mAh cm^{-2} at the current density of 1 mA cm^{-2}, and b) with an areal charge of 4 mAh cm^{-2} at the current density of 4 mA cm^{-2}. The cutoff voltage in each cycle was 1 V. The inset images show the voltage profiles at different cycles.

voltage dropped below 0 V. Cu had a higher overpotential compared to LHC/BN and LHC, due to the higher resistance of plating Li on the Cu. The plating process of LHC was much shorter than that of LHC/BN, which suggested that LHC had lower Li capacity than the LHC/BN. After cycling for 150 cycles, there was no obvious change in voltage profiles of LHC/BN and LHC electrodes, indicating high Li stability of both electrodes. However, at the 440th cycle, LHC showed decreased plating time and fluctuating curve due to dendrite formation, consistent with the limited stabilization capability of LHC described previously. In comparison, the stripping process of Cu electrode was much shorter and less stable compared to the other two electrodes. The instability of Cu electrode was due to the continuous growth of dendrite which consumed a large portion of electrolyte during the repeated breaking-down and reforming of SEI.

Higher current density can cause more Joule heat during the plating/stripping process, and the heat dissipation will have a significant effect on the Li deposition. The Coulombic efficiency of the three electrodes at higher current density of 4 mA·cm^{-2} with a higher areal charge of 4 mAh·cm^{-2} was measured (Figure 4b). At high current density, the LHC/BN was more advantageous in terms of Li deposition and resistance. The Coulombic efficiency of the LHC/BN electrode was stable at 97.8% for more than 350 cycles. In comparison, the Coulombic efficiency of LHC could maintain 96% for 300 cycles without good stability. And Cu electrode showed a fast decay from 96% to 53% in the first 50 cycles. The inset images show the voltage profiles of the 5th, 50th, and 300th cycle, respectively. At the 5th cycle, the Cu showed the highest overpotential while the LHC/BN showed the lowest. And the amount of Li plated onto Cu and LHC are smaller than that onto LHC/BN. After the first 50 cycles, the stripping time of Cu electrode reduced significantly, leading to a reduced Coulombic efficiency, while that of the LHC/BN and LHC did not change. After 300 cycles, the voltage profile of LHC/BN showed no significant change. However, the stripping time of the LHC electrode was over 1 h, giving rise to a Coulombic efficiency of over 100%, as a consequence of uneven Li plating/stripping. In conclusion, compared with the Cu electrode, both LHC and LHC/BN had a lower resistance in Li deposition and higher Coulombic efficiency. BN in the structure further reduced the resistance and improved reversibility of the plating/stripping process. The improvement by LHC/BN was more striking at higher current density. So far it has been rare for the reported Li hosts to achieve such a high Coulombic efficiency with excellent stability over long cycling, as compared in Table S1 in the Supporting Information.

The above investigation on Coulombic efficiency was to learn the plating/stripping behavior of Li on the host materials. To study the electrochemical behavior of the different structures as anode materials, a fixed amount of Li was predeposited to LHC/BN, LHC, and Cu to form the LHC/BN-Li, LHC-Li, and Cu-Li anodes, respectively. **Figure 5**a and its insets compare the

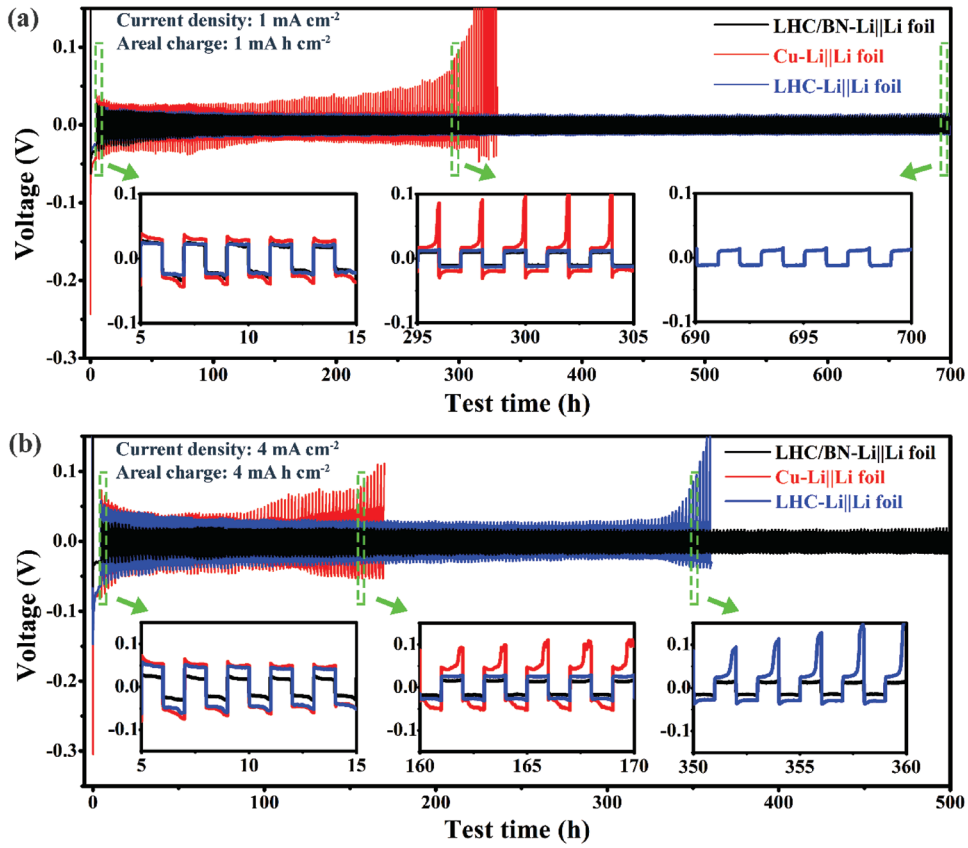

Figure 5. Comparison of cycling performance between LHC/BN-Li, LHC-Li, and Cu-Li anodes (a) at the current density of 1 mA cm^{-2} with an areal charge of 1 mAh cm^{-2}, and (b) at the current density of 4 mA cm^{-2} with areal charge of 4 mAh cm^{-2}. The inset images were the expansions at different cycle range.

potential profiles of LHC/BN-Li, LHC-Li, and Cu-Li electrodes which were predeposited with 5 mAh·cm^{-2} Li at a current density of 1 mA·cm^{-2}. And LHC/BN-Li, LHC-Li, and Cu-Li electrodes were tested for stripping/plating at 1 mAh·cm^{-2} at the same current density subsequently. At lower current density, the LHC/BN-Li and LHC-Li had no obvious differences in the Li plating/stripping behavior. Both electrodes exhibited stable cycling after 700 h with flat voltage plateau and small voltage range between −15 and 15 mV. In contrast, the voltage profile of Cu-Li anode showed a large hysteresis and gradual increase in overpotential during cycling. And the voltage hysteresis of Cu-Li suddenly increased to over 100 mV after 300 h, which was due to the huge resistance caused by the continuous formation of the dendrite and the insulating SEI. These results proved that the layered structure can effectively suppress the dendrite formation.

However, when the current density for Li predeposition was increased to 4 mA·cm^{-2} with a concurrent increase in the amount of Li deposited to 20 mAh·cm^{-2}, the differences between LHC/BN-Li and LHC-Li were more distinct (Figure 5b). The LHC/BN-Li showed a stable cycling for 500 h with a small voltage hysteresis and a small potential range between −20 and 20 mV. In contrast, the LHC-Li anode maintained a stable cycling for 320 h and then the voltage hysteresis increased to over 100 mV. As expected, the Cu-Li exhibited the largest potential variation between −73 and 73 mV in the initial cycle, and a fast failure after 175 h of cycling. These results agreed with the previous Coulombic efficiency measurements. At a higher current density, more Joule heat was generated on the surface of Li anode. The LHC/BN-Li anode displayed more favorable stability of Li deposition/dissolution than the BN-free anode because of better capability of heat dissipation of BN. Compared with other hosted Li anodes reported recently, LHC/BN-Li showed a much longer and stable cycling lifespan at a high current density (Table S2, Supporting Information).

Electrochemical impedance spectroscopy (EIS) was used to confirm the fast charge transfer of the LHC/BN electrodes (Figure S9, Supporting Information). Before Li deposition, the Cu and LHC electrodes showed larger semicircle at high frequency region in the Nyquist plot than LHC/BN, indicating higher interfacial resistance. After Li deposition, the interfacial resistance of all three electrodes decreased. The higher resistance in Cu-Li and LHC-Li was a result of heterogeneous Li deposition and uneven electrolyte distribution across the surface of the electrode. The lower interfacial resistance of LHC/BN suggested a higher charge transfer kinetics, consistent with the results discussed above.

To further understand the advantages of the unique layered structure of LHC/BN and the effect of thermal distribution on suppressing dendrite, morphology evolution of LHC/BN-Li, LHC-Li, and Cu-Li anodes before and after cycling were recorded by SEM. **Figure 6**a schematically displays the

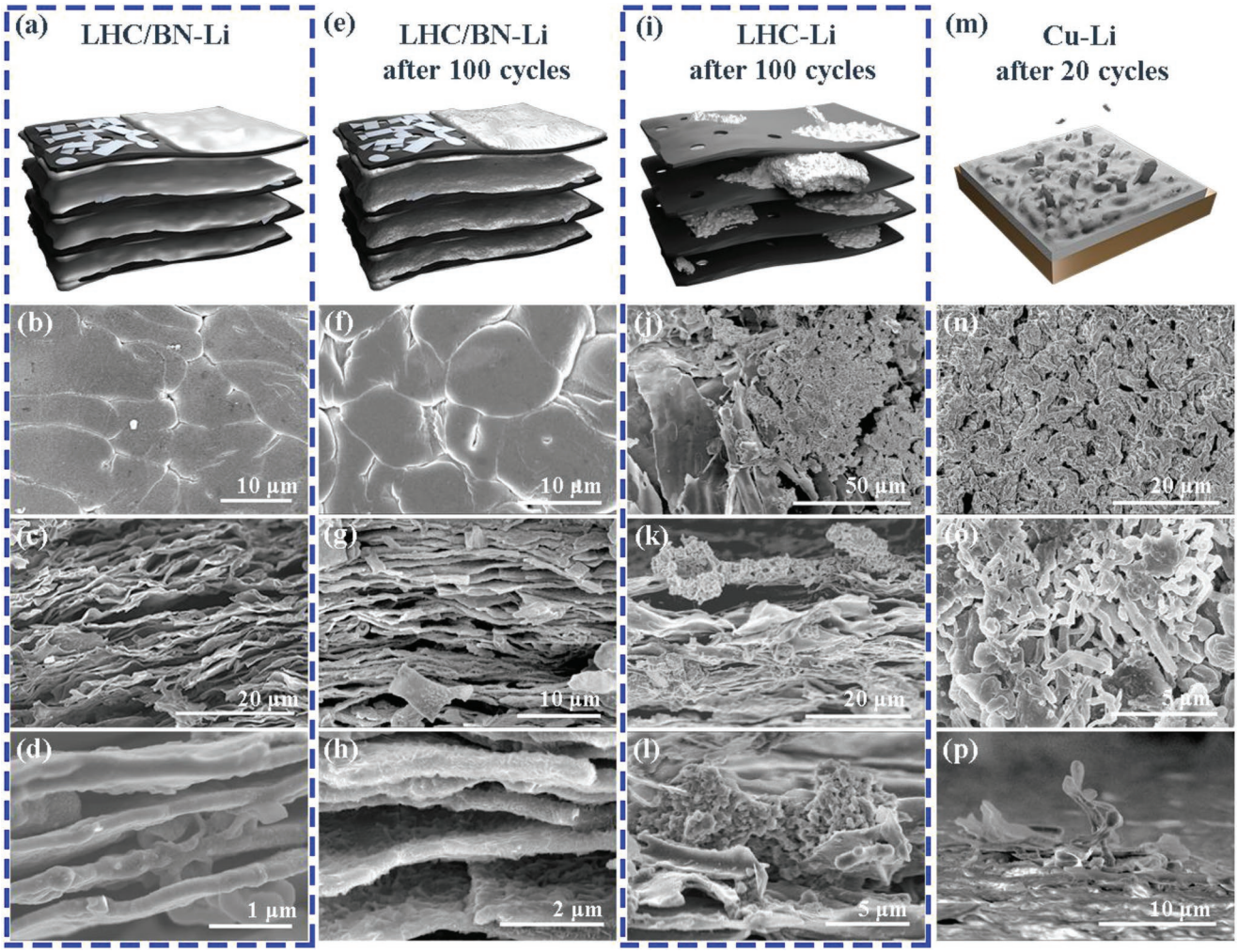

Figure 6. Schematics and SEM images of morphology evolution of LHC/BN-Li, LHC-Li, and Cu-Li anodes before and after cycling. a) Schematic of Li deposition in LHC/BN-Li before cycling and (b) SEM of top view, (c) SEM of sectional view and (d) SEM expansion of sectional view of LHC/BN-Li anode before cycling. e) Schematic of uniform Li distribution in LHC/BN-Li after cycling and (f) SEM of top view, (g) SEM of sectional view and (h) SEM of expansion of sectional view of LHC/BN-Li anode after 100 cycles. i) Schematic of non-uniformly distributed Li in LHC-Li anode after 100 cycles and (j) SEM of top view, (k) SEM of sectional view and (l) SEM expansion of sectional view of LHC-Li anode after 100 cycles. m) Schematic of Li dendrites of Cu-Li anode after 20 cycles and (n) SEM of top view, (o) SEM expansion of top view and (p) SEM of a vertically grown dendrite of Cu-Li anode after 20 cycles.

structure of LHC/BN-Li anode before cycling. During the Li deposition process, the photon transmission process within the overlapped BN nanosheets is fast, which is the reason for the high thermal diffusivity. As shown in Figure 6b, after Li plating for 5 h at a current density of 4 $mA \cdot cm^{-2}$, the LHC/BN-Li anode showed a uniform and smooth surface. From the cross-section images (Figure 6c,d), Li was uniformly deposited on both sides of carbon layer, and the interlayered gaps were large enough to host more Li. In comparison, the LHC-Li before cycling showed a coarse surface coverage with Li (Figure S10, Supporting Information). As for the Cu-Li electrode before cycling, Li deposition was uneven and dendrites were clearly seen (Figure S11, Supporting Information). After stripping/plating for 100 cycles at a current density of 4 $mA \cdot cm^{-2}$ with an areal charge of 4 $mAh \cdot cm^{-2}$, the LHC/BN-Li and LHC-Li were very different in morphology. LHC/BN-Li anode can still maintain good structural stability and suppress dendrite after 100 cycles as illustrated in Figure 6e. According to SEM image, Li maintained a very smooth and dense surface after 100 cycles (Figure 6f). And the layered structure was well-maintained, with no obvious dendrite formation (Figure 6g,h).

Different from the BN-containing sample, after 100 cycles, LHC-Li did not show uniformly covered Li, as schematically illustrated in Figure 6i. In the SEM image of LHC-Li, a bare carbon layer with no Li plated was observed (Figure 6j). From the cross-section images in Figure 6 k,l, it is obvious that the interlayer gap was filled with dendrite and the dendrite even penetrated through the layers.

The morphology of Cu-Li after cycling at the same current density and areal capacity for 20 cycles was also recorded, and severe dendrites formation was observed. As illustrated in Figure 6m, the limited contact area between the electrode and electrolyte, as well as the non-uniform Li ion distribution all contributed to severe dendrite formation at high current

density. After only 20 cycles, as shown in Figure 6n, the surface of the Cu-Li became very coarse and porous, where dendrite wires with a diameter of 2 µm tangled together and randomly grew. At higher magnification (Figure 6o), thinner dendrite wires with a diameter of 200 µm were also observed. As shown in Figure 6p, sharp dendrites which grew in the vertical direction from the surface of Cu-Li anode can potentially pierce the separator and cause short circuit.

To demonstrate the potential of practical use of LHC/BN in a full cell, and evaluate the effect of thermal management on the performance of the cell, full cells with $LiFePO_4$ as the cathode were assembled using LHC/BN-Li, LHC-Li, and Cu-Li as the anode, respectively. The rate performance of the full cell is shown in **Figure 7**a. At low current rate of 0.2 C, the LHC/BN-Li, LHC-Li, and Cu-Li full cells showed similar capacity of 152, 149, and 147 mAh g^{-1}, respectively, on the first cycle. However, as the discharge/charge rate increased to 10 C (corresponding to 4.5 mA·cm^{-2} in areal current density), the LHC/BN-Li full cell achieved the highest capacity of 84 mAh·g^{-1}, and the LHC-Li and Cu-Li full cells only achieved 74 and 55 mAh g^{-1}, respectively. As a comparison, pure Li foil could only achieve 5 mAh·g^{-1} at 10 C as an anode in the full cell due to low Li ion accessibility at high current density in the bulk Li foil (Figure S12, Supporting Information). The rate performance agreed well with the previous results that Li could uniformly plate and strip on the layered porous structure with more even heat and current distribution. The 3D structure was more advantageous at high current density. Figure 7b and 7c compare the galvanostatic charge/discharge profiles of full cells at 0.2 and 10 C, respectively. The LHC/BN-Li had the smallest voltage difference between charge and discharge reaction plateaus, indicating lowest polarization and improved reaction kinetics. Meanwhile, as shown in Figure S13 in the Supporting Information, the smallest peak separation in the

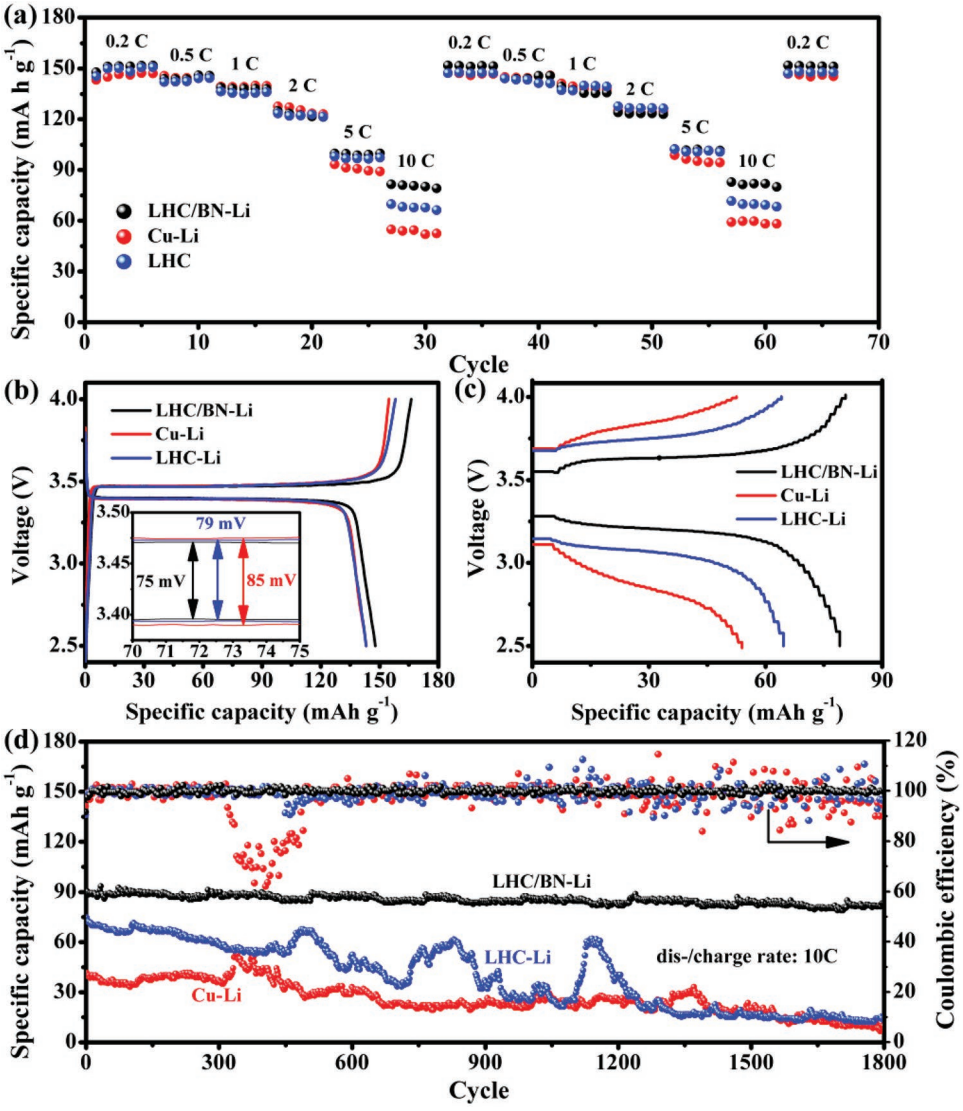

Figure 7. Performance of full cells with $LiFePO_4$ cathode and LHC/BN-Li, LHC-Li, and Cu-Li anode, respectively. a) Rate capabilities at various rates from 0.2 to 10 C. b) Galvanostatic charge/discharge profiles at 0.2 C and (c) galvanostatic charge/discharge profiles at 10 C. The inset shows the expanded profiles at 0.2 C. d) The long-term cycling behavior at 10 C.

cyclic voltammetry (CV) curves also indicates the lowest polarization in LHC/BN-Li cell, which was consistent with the conclusions of abovementioned discussion. To further clarify the effect of heat distribution, full cells were tested at a rate of 10 C, as shown in Figure 7d. Remarkably, the LHC/BN-Li full cell exhibited the highest capacity of 90 mAh g^{-1} at the initial cycle, and a superior capacity retention of 92% for 1800 cycles. On the other hand, the LHC-Li and Cu-Li full cells achieved a capacity of 73 and 41 mAh g^{-1} at the initial cycle, respectively, and the capacity deteriorated to 15 and 7 mAh g^{-1} after 1800 cycles, respectively. Furthermore, the LHC/BN-Li full cell showed a high Coulombic efficiency (>99%) in the long-term cycling, while LHC-Li and Cu-Li showed much worse stability as the Coulombic efficiency exceeded 100% at some cycles. Table S3 in the Supporting Information summarizes the full cell performance reported with $LiFePO_4$ as cathode and different hosted Li as anode, and the LHC/BN is obviously superior to others in cycling stability and rate capability.

In summary, this work designed a novel 3D Li scaffold with enhanced thermal diffusivity and superior ion accessibility to stabilize the Li metal anode. With this novel structure, the local areal current density can be significantly reduced when the electrode was tested at high current load. More importantly, effective thermal dissipation can lead to uniform Li deposition. Therefore, dendrite formation can be effectively impeded. As a result, the LHC/BN electrode in this work demonstrated a high Li stripping/plating Coulombic efficiency of 98% for 500 cycles at a current density of 1 mA·cm^{-2} and 97.8% for 350 cycles at a current density of 4 mA·cm^{-2}, respectively. The novel Li metal anode showed excellent cyclic stability for 700 h at a current density of 1 mA·cm^{-2}, and for 500 h at a higher current density of 4 mA·cm^{-2}. In a full cell test with LHC/BN as anode and $LiFePO_4$ as cathode, a high specific capacity of 90 mAh·g^{-1} at 10 C (corresponding to 4.5 mA cm^{-2}) at the initial cycle was achieved with a high capacity retention of 92% after 1800 cycles. In contrast, the full cell with Li foil anode and $LiFePO_4$ cathode showed poor cycling stability and the capacity decayed to 15 mAh·g^{-1} after 1800 cycles. The SL-derived LHC/BN structure with the capability of thermal management is a promising Li host for the use of Li metal batteries.

Supporting Information

Supporting Information is available from the Wiley Online Library or from the author.

Acknowledgements

H.Z. acknowledges the financial startup support from Northeastern University. The authors thank the Kostas Research Institute at Northeastern University for the use of TEM facilities. The authors thank Dr. Gunnar Henriksson in KTH Royal Institute of Technology for kindly providing the ligninsulfonate. The authors acknowledge the use of XRD facilities under the auspices of the Northeastern University Center for Renewable Energy Technology (NUCRET). D.C. acknowledges the China scholarship council for supporting a visit to Northeastern University. The authors also thank Dr. Gang Chen and Jiawei Zhou in Massachusetts Institute of Technology for their help on the thermal diffusivity measurement.

Conflict of Interest

The authors declare no conflict of interest.

Keywords

boron nitride, dendrite, ligninsulfonate, lithium metal, thermal distribution

Received: December 14, 2018
Revised: January 11, 2019
Published online:

[1] a) P. G. Bruce, S. A. Freunberger, L. J. Hardwick, J.-M. Tarascon, *Nat. Mater.* **2012**, *11*, 19; b) H. Kim, G. Jeong, Y.-U. Kim, J.-H. Kim, C.-M. Park, H.-J. Sohn, *Chem. Soc. Rev.* **2013**, *42*, 9011; c) D. Lin, Y. Liu, Y. Cui, *Nat. Nanotechnol.* **2017**, *12*, 194.

[2] a) E. Peled, *J. Electrochem. Soc.* **1979**, *126*, 2047; b) P. Albertus, S. Babinec, S. Litzelman, A. Newman, *Nat. Energy* **2018**, *3*, 16.

[3] a) G. Zheng, S. W. Lee, Z. Liang, H.-W. Lee, K. Yan, H. Yao, H. Wang, W. Li, S. Chu, Y. Cui, *Nat. Nanotechnol.* **2014**, *9*, 618; b) W. Xu, J. Wang, F. Ding, X. Chen, E. Nasybulin, Y. Zhang, J.-G. Zhang, *Energy Environ. Sci.* **2014**, *7*, 513; c) Y. Lu, Z. Tu, L. A. Archer, *Nat. Mater.* **2014**, *13*, 961.

[4] a) Y. Liu, Y. Qiao, Y. Zhang, Z. Yang, T. Gao, D. Kirsch, B. Liu, J. Song, B. Yang, L. Hu, *Energy Storage Mater.* **2018**, *12*, 197; b) W. Luo, L. Zhou, K. Fu, Z. Yang, J. Wan, M. Manno, Y. Yao, H. Zhu, B. Yang, L. Hu, *Nano Lett.* **2015**, *15*, 6149.

[5] a) H. J. S. Sand, *London, Edinburgh Dublin Philos. Mag. J. Sci.* **1901**, *1*, 45; b) F. Shen, F. Zhang, Y. Zheng, Z. Fan, Z. Li, Z. Sun, Y. Xuan, B. Zhao, Z. Lin, X. Gui, X. Han, Y. Cheng, C. Niu, *Energy Storage Mater.* **2018**, *13*, 323; c) C. Shang-Sen, L. Yongchang, S. Wei-Li, F. Li-Zhen, Z. Qiang, *Adv. Funct. Mater.* **2017**, *27*, 1700348; d) L. Sufu, X. Xinhui, Z. Yu, D. Shengjue, Y. Zhujun, Z. Liyuan, C. Xin-Bing, W. Xiuli, Z. Qiang, T. Jiangping, *Adv. Energy Mater.* **2018**, *8*, 1702322.

[6] A. M. Hafez, J. Yucong, S. Jianjian, M. Yi, C. Daxian, L. Yuanyue, Z. Hongli, *Adv. Mater.* **2018**, *30*, 1802156.

[7] a) J. Xie, L. Liao, Y. Gong, Y. Li, F. Shi, A. Pei, J. Sun, R. Zhang, B. Kong, R. Subbaraman, J. Christensen, Y. Cui, *Sci. Adv.* **2017**, *3*, eaao3170; b) J. Shim, H. J. Kim, B. G. Kim, Y. S. Kim, D.-G. Kim, J.-C. Lee, *Energy Environ. Sci.* **2017**, *10*, 1911; c) C. Jin, H. Xingyi, Z. Yingke, J. Pingkai, *Adv. Funct. Mater.* **2017**, *27*, 1601741.

[8] a) I. Jo, M. T. Pettes, J. Kim, K. Watanabe, T. Taniguchi, Z. Yao, L. Shi, *Nano Lett.* **2013**, *13*, 550; b) Q. Li, G. Z. Zhang, F. H. Liu, K. Han, M. R. Gadinski, C. X. Xiong, Q. Wang, *Energy Environ. Sci.* **2015**, *8*, 922.

[9] H. Zhu, Y. Li, Z. Fang, J. Xu, F. Cao, J. Wan, C. Preston, B. Yang, L. Hu, *ACS Nano* **2014**, *8*, 3606.

[10] a) H. Renault, A. Alber, N. A. Horst, A. Basilio Lopes, E. A. Fich, L. Kriegshauser, G. Wiedemann, P. Ullmann, L. Herrgott, M. Erhardt, E. Pineau, J. Ehlting, M. Schmitt, J. K. C. Rose, R. Reski, D. Werck-Reichhart, *Nat. Commun.* **2017**, *8*, 14713; b) H. Zhu, W. Luo, P. N. Ciesielski, Z. Fang, J. Y. Zhu, G. Henriksson, M. E. Himmel, L. Hu, *Chem. Rev.* **2016**, *116*, 9305; c) A. Mukhopadhyay, J. Hamel, R. Katahira, H. Zhu, *ACS Sustainable Chem. Eng.* **2018**, *6*, 5394; d) Y. Matsushita, S. Yasuda, *Bioresour. Technol.* **2005**, *96*, 465.

[11] W. Liu, C. Zhao, R. Zhou, D. Zhou, Z. Liu, X. Lu, *Nanoscale* **2015**, *7*, 9919.
[12] a) D. Lin, Y. Liu, Z. Liang, H.-W. Lee, J. Sun, H. Wang, K. Yan, J. Xie, Y. Cui, *Nat. Nanotechnol.* **2016**, *11*, 626; b) H. Li, Y. Hou, F. Wang, M. R. Lohe, X. Zhuang, L. Niu, X. Feng, *Adv. Energy Mater.* **2017**, *7*, 1601847; c) C. Wang, X. Chen, B. Wang, M. Huang, B. Wang, Y. Jiang, R. S. Ruoff, *ACS Nano* **2018**, *12*, 5816; d) P. Zhang, J. Li, L. Lv, Y. Zhao, L. Qu, *ACS Nano* **2017**, *11*, 5087.
[13] X. Geng, Y. Zhang, L. Jiao, L. Yang, J. Hamel, N. Giummarella, G. Henriksson, L. Zhang, H. Zhu, *ACS Sustainable Chem. Eng.* **2017**, *5*, 3553.
[14] S. Bhattacharjee, *J. Controlled Release* **2016**, *235*, 337.
[15] a) Y. Zhang, B. Liu, E. Hitz, W. Luo, Y. Yao, Y. Li, J. Dai, C. Chen, Y. Wang, C. Yang, H. Li, L. Hu, *Nano Res.* **2017**, *10*, 1356; b) B. D. Adams, J. Zheng, X. Ren, W. Xu, J.-G. Zhang, *Adv. Energy Mater.* **2018**, *8*, 1702097.